

Electrostatic interactions in atomistic and machine-learned potentials for polar materials

Lorenzo Monacelli and Nicola Marzari

*Theory and Simulation of Materials (THEOS), and National Centre for Computational Design and Discovery of Novel Materials (MARVEL),
École Polytechnique Fédérale de Lausanne, 1015 Lausanne, Switzerland*

(Dated: December 3, 2024)

Long-range electrostatic interactions critically affect polar materials. However, state-of-the-art atomistic potentials, such as neural networks or Gaussian approximation potentials employed in large-scale simulations, often neglect the role of these long-range electrostatic interactions. This study introduces a novel model derived from first principles to evaluate the contribution of long-range electrostatic interactions to total energies, forces, and stresses. The model is designed to integrate seamlessly with existing short-range force fields without further first-principles calculations or retraining. The approach relies solely on physical observables, like the dielectric tensor and Born effective charges, that can be consistently calculated from first principles. We demonstrate that the model reproduces critical features, such as the LO-TO splitting and the long-wavelength phonon dispersions of polar materials, with benchmark results on the cubic phase of barium titanate (BaTiO_3).

I. INTRODUCTION

In polar materials, displacing an ion from equilibrium generates an electric dipole. The resulting electric field decays as the inverse of the cube of the distance and interacts with local dipoles generated by far-away ionic displacements. While these long-range electrostatic interactions are screened in metals, and their role becomes relevant only when accounting for ionic dynamics[1, 2], in the absence of electrons in the conduction band long-range electric fields survive down to zero frequency, thus playing a fundamental role in the phenomenology of insulators. This includes the splitting between longitudinal and transverse optical phonons at long wavelengths (LO-TO splitting)[3–6], affecting in turn all thermodynamic properties related to phonon dispersions, such as thermal expansion, heat capacity, lattice thermal conductivity, and Raman and IR spectra. First-principles simulations include long-range electrostatic interactions [4, 7] when considering perturbations of finite wavevector, where the phonons can be evaluated either by finite-differences[8] or density-functional perturbation theory (DFPT)[4]. At Γ ($\mathbf{q} = 0$), the contribution of electrostatic interaction is nonanalytic, as $\mathbf{q} = 0$ periodic displacements produce macroscopic polarizations resulting in a dynamical matrix for phonons dependent on the direction of the \mathbf{q} vector as it approaches Γ . This nonanalytic behavior of lattice force constants near Γ constitutes a challenge in modeling efficient force fields for polar materials, as it originates from the cubic power-law decay of electrostatic forces and can not be captured if the interaction is truncated over a finite distance.

Thanks to the advances in machine learning technologies, many excellent tools to fit atomistic potentials from small sets of high quality *ab initio* calculations have emerged[9–14], paving the way to the simulation of large-scale materials with hundreds of millions of atoms with an accuracy close to first principles

methods[15, 16]. However, the most commonly employed machine-learning potentials neglect the long-range electrostatic interactions, resulting in a smooth \mathbf{q} dependence of the atomic force constant matrix around Γ . This is because the force field parametrizations account only for local atomic environments, and the first principles training data are evaluated on periodic boundary conditions that lack long-range contributions. The question arises of what should be fitted and how electrostatics can be recovered. Several methods have been developed to overcome this issue. Some approaches, the so-called second and third-generation machine-learning potential[17], split the energy expression into a short and long-range part, explicitly accounting for electrostatic interactions between point charges dependent on the local nuclear environment[18–23]. These models suffer from the need for extra training data like partial atomic charges that, while easy to extract from DFT simulations, are not physical observables and ubiquitously defined[19]. To overcome this issue, different methods have been proposed to rely on physical observables, like the electron densities[24], the Wannier functions[25], and polarization[26, 27], which can be rigorously defined through the modern theory of polarization[28–30]. These approaches have also been augmented to describe charge relocalization by solving a charge equilibration equation self-consistently, the so-called 4th generation scheme[31, 32]. While promising, these procedures require new first-principles calculations to store the extra information needed for the training, hampering the reuse of energy/forces data generated, for example, from previous first-principles calculations of molecular dynamics (FPMD). A different strategy introduces long-range descriptors of atomic coordinates[33], also achieved by message-passing neural architectures architectures[34]. While very promising, especially in their ability to account for macroscopic rearrangement of the electron charge in the system, these models need a training set

with sufficiently large simulation cells to sample long-range interactions[27, 33, 34], preventing the employment of small simulation cells in the training data.

This work presents instead a comprehensive first-principles approach designed to integrate long-range interactions seamlessly with existing short-range force fields in polar condensed matter systems. The method accurately calculates total energies, forces, and stress tensors, and it is grounded solely on a select set of well-established first-principles properties of the material in its equilibrium state.

II. RESULTS

A. Electrostatic energy

The coupling between dipoles is the leading term of the long-range electrostatic interactions in neutral systems. Each dipole $\boldsymbol{\mu}_i$ generates an electric field $\mathbf{E}(\mathbf{R}_i)$ decaying as the inverse of the cube of the distance, which interacts with other dipoles as

$$\mathcal{E} = -\frac{1}{2} \sum_{i=1}^N \mathbf{E}(\mathbf{R}_i) \cdot \boldsymbol{\mu}_i, \quad (1)$$

where bold symbols represent vectors and matrices; the $\frac{1}{2}$ in Eq. (1) prevents double counting when summing over all the atoms.

The overall dipole moment $\boldsymbol{\mu}$ of the crystal can be rigorously defined through the modern theory of polarization[28–30]. Here, we can define the atomic dipole $\boldsymbol{\mu}_i$ as the contribution to the overall dipole moment $\boldsymbol{\mu}$ given by the displacement of atom i

$$Z_{i\alpha\beta} = \frac{\partial \mu_\alpha}{\partial R_{i\beta}}, \quad \mu_\alpha(\mathbf{R}) = \mu_\alpha^{(0)} + \sum_{i=1}^N \mu_{i\alpha}(\mathbf{R}), \quad (2)$$

$$\mu_{i\alpha}(\mathbf{R}) = \sum_{\beta} Z_{i\alpha\beta} (R_{i\beta} - \mathcal{R}_{i\beta}), \quad (3)$$

where μ_α and $\mu_{i\alpha}$ are the α Cartesian component of the dipole moment per cell of the total system and the one of the i -th atom, respectively. $Z_{i\alpha\beta}$ is the Born effective charges tensor, \mathcal{R}_i is the equilibrium position of the i -th atom, and $\boldsymbol{\mu}^{(0)}$ is the total dipole moment when atoms are in the equilibrium position, defined up to a quantum of polarization. We identify the atoms with Latin indices and the Cartesian components with Greek ones. To parametrize the electric field generated by the dipoles of Eq. (3), we define an auxiliary distribution of spherical charges reproducing a dipole $\boldsymbol{\mu}_i$ on each atom. In particular, each dipole consist of two charges q of opposite signs and at a distance d as

$$\boldsymbol{\mu} = q\mathbf{d}. \quad (4)$$

The modulus of the dipole qd leaves an arbitrary choice on the values for q and d , which, however, only affects terms of the multipole expansions beyond the dipole and, thus, disappears from the final expression for the energy and its derivatives (forces and stresses) in the dipole limit (Appendix C).

By exploiting this system of charges, we define a charge density $\rho(\mathbf{r})$ that reproduces the correct long-range dipole-dipole interactions but sufficiently slow-varying to smear out short-range interactions.

$$\rho(\mathbf{r}) = \sum_{j=1}^{2N} \frac{q_j}{\sqrt{8\pi^3}\eta^2} \exp\left[-\frac{(\mathbf{r} - \tilde{\mathbf{R}}_j)^2}{2\eta^2}\right], \quad (5)$$

where $\tilde{\mathbf{R}}_j$ is the position of the charge q_j . We derive an expression for $\tilde{\mathbf{R}}_j$ in Appendix A. The η parameter is the short-range smearing. This way, the resulting force field does not affect energies and its derivatives computed on periodic cells with a linear size smaller than η . This approach is highly practical as it enables adjusting η in such a way that the charge density electrostatic interactions do not affect training data defined in small cells employed to develop the short-range machine-learning interatomic potential. Consequently, this makes the potential reusable in conjunction with our charge model, eliminating the need for retraining.

The electric field produced by a polar charge distribution, as in Eq. (5), is slowly and conditionally convergent as it generates a macroscopic charge on the surface of the solid. The problem is solved in Fourier space with the Ewald summation for a 3D bulk material (details in Appendix B):

$$\mathbf{E}(\mathbf{r}) = \frac{i}{\Omega} \sum_{\substack{j \\ k_j \neq 0}} \frac{\mathbf{k}_j e^{-\frac{\eta^2 k_j^2}{2}} e^{i\mathbf{k}_j \cdot \mathbf{r}}}{\sum_{\alpha\beta} k_{j\alpha} \epsilon_{\alpha\beta} k_{j\beta}} S(\mathbf{k}_j), \quad (6)$$

where Ω is the supercell volume, i is the imaginary unit coming from the Maxwell-Equations in Fourier space, and $S(\mathbf{k})$ is the structure factor associated to the auxiliary charge system:

$$S(\mathbf{k}) = \sum_{j=1}^{2N} q_j e^{-i\mathbf{k} \cdot \tilde{\mathbf{R}}_j}. \quad (7)$$

The values assumed by the \mathbf{k} vectors are constrained to be multiples of the reciprocal lattice:

$$\mathbf{k}_{(l,m,n)} = l\mathbf{a} + m\mathbf{b} + n\mathbf{c}, \quad (8)$$

where \mathbf{a} , \mathbf{b} , and \mathbf{c} are the reciprocal lattice vectors of the periodic supercell, and l, m, n go from $-\infty$ to ∞ , excluding $\mathbf{k} = 0$. Additional care must be taken if the charge distribution is not defined in bulk systems, as in 2D materials or 1D chains, where Eq. (6) is no longer valid and a nonuniform spatial dependency of the dielectric tensor needs to be taken into account[7, 35, 36].

Integrating the electrostatic energy of Eq. (5) with the expression of the electric field (Eq. 6), we get the total energy (see Appendix C for details on the calculation)

$$\mathcal{E}(\mathbf{R}) = \frac{1}{2} \sum_{ij\alpha\beta\mu\nu} (R_{i\alpha} - \mathcal{R}_{i\alpha})(R_{j\mu} - \mathcal{R}_{j\mu}) \frac{Z_{i\beta\alpha} Z_{j\nu\mu}}{\Omega} \cdot \sum_{\substack{k \\ k \neq 0}} \frac{k_\beta k_\nu e^{-\frac{\eta^2 k^2}{2}}}{\sum_{\mu\nu} k_\mu \epsilon_{\mu\nu} k_\nu} e^{-i\mathbf{k}(\mathbf{R}_j - \mathbf{R}_i)}. \quad (9)$$

Eq. (9) is the central result of this work. It defines the energy contribution of long-range dipole-dipole interactions and depends explicitly on the atomic positions. Notably, the expression for the energy only depends on physical observables, as the arbitrary (nonphysical) values of the atomic charges q_j and their positions $\tilde{\mathbf{R}}_j$ cancel out in the dipole limit. The computation of Eq. (9) requires first-principles quantities like the high-frequency dielectric tensor ϵ and effective charges \mathbf{Z} at the equilibrium position \mathcal{R} , and the only free parameter is the smearing factor η .

B. Forces and stress tensor

Long-range forces are obtained by deriving the expression for the electrostatic energy:

$$f_{i\alpha} = -\frac{\partial \mathcal{E}}{\partial R_{i\alpha}}. \quad (10)$$

$$f_{i\alpha} = - \sum_{j\beta\mu\nu} (R_{j\mu} - \mathcal{R}_{j\mu}) \frac{Z_{i\beta\alpha} Z_{j\nu\mu}}{\Omega} \cdot \sum_{\substack{k \\ k \neq 0}} \frac{k_\beta k_\nu e^{-\frac{\eta^2 k^2}{2}}}{\sum_{\mu\nu} k_\mu \epsilon_{\mu\nu} k_\nu} \cos[\mathbf{k}(\mathbf{R}_j - \mathbf{R}_i)] + \sum_{j\beta\gamma\mu\nu} (R_{i\gamma} - \mathcal{R}_{i\gamma})(R_{j\mu} - \mathcal{R}_{j\mu}) \frac{Z_{i\beta\gamma} Z_{j\nu\mu}}{\Omega} \cdot \sum_{\substack{k \\ k \neq 0}} \frac{k_\alpha k_\beta k_\nu e^{-\frac{\eta^2 k^2}{2}}}{\sum_{\mu\nu} k_\mu \epsilon_{\mu\nu} k_\nu} \sin[\mathbf{k}(\mathbf{R}_j - \mathbf{R}_i)] \quad (11)$$

The only term that survives in the long-wavelength limit is the first one, as the second one goes as k^2 for small values of k . However, in the actual implementation, we kept the full expression Eq. (11) to guarantee that the numerical value of the forces coincides with the gradient of the total energy. The partition of the total dipole moment of the cell into local atomic dipoles operated in Eq. (3) violates the translational invariance of the system, introducing a nonzero net force in the center of mass. However, the overall translational invariance can be easily restored directly in the total energy (Eq. 9) by redefining the centroids \mathcal{R} as a function of the atomic

positions to eliminate any rigid translation from the displacement $\mathbf{R} - \mathcal{R}$ (see Eq. D2). In Appendix D, we show how this choice restores the full translational invariance, correcting forces and stresses to satisfy the translational acoustic sum rule.

The stress tensor σ quantifies the energy to deform the lattice. Its computation is required in variable cell simulations, like NPT molecular dynamics or in the stochastic self-consistent harmonic approximation (SSCHA)[37–41], and is fundamental in evaluating thermal expansion and the equation of state; it is defined

$$\sigma_{\alpha\beta} = -\frac{1}{\Omega} \frac{\partial \mathcal{E}}{\partial \varepsilon_{\alpha\beta}}, \quad (12)$$

where the strain tensor ε is a symmetric matrix. Atomic positions (clamped ions) follow strain as

$$R'_\alpha(\varepsilon) = R_\alpha + \sum_\beta \varepsilon_{\alpha\beta} R_\beta. \quad (13)$$

Since strain changes the lattice parameters, also the reciprocal vectors \mathbf{k} are affected as

$$k'_\alpha(\varepsilon) = k_\alpha - \sum_\beta \varepsilon_{\alpha\beta} k_\beta; \quad (14)$$

therefore, the scalar product between \mathbf{R} and \mathbf{k} remains unchanged under strain. The volume is also affected by the strain as

$$\Omega'(\varepsilon) = \Omega \left(1 + \sum_{\alpha=1,3} \varepsilon_{\alpha\alpha} \right). \quad (15)$$

The expression of the stress can be easily obtained by substituting $\Omega'(\varepsilon)$, $\mathbf{R}'(\varepsilon)$, $\mathcal{R}'(\varepsilon)$, and $\mathbf{k}'(\varepsilon)$ in the electrostatic energy (Eq. 9), and evaluating the Jacobian of Eq. (12) by applying the differential chain rule recursively. Our implementation achieved the final result by exploiting the algorithmic differentiation as implemented in the Julia library ForwardDiff.jl[42].

C. LO-TO splitting

One of the essential features that the long-range electrostatic force field must reproduce is the correct phonon dispersion in the long-wavelength limit, where, in bulk 3D material, the cubic decay of the dipole-dipole forces with the inverse of the distance gives rise to a discontinuity of the dynamical matrix at Γ , where the $\mathbf{q} \rightarrow 0$ limit is dependent on the direction $\mathbf{q}/|\mathbf{q}|$, and consequently to the LO-TO splitting (see ref.[43] and ref.[36] for the 2D and 1D case, respectively). To prove that the model correctly reproduces the phonon dispersions in the $\mathbf{q} \rightarrow 0$ limit, we derived the expression of the interatomic force constant matrix

$$\Phi_{\alpha\beta}^{ij} = \frac{d^2 \mathcal{E}}{dR_{i\alpha} dR_{j\beta}} = -\frac{df_{i\alpha}}{dR_{j\beta}}. \quad (16)$$

Restricting ourselves to the equilibrium position $\mathbf{R} = \mathcal{R}$, the only surviving term is:

$$\Phi_{\alpha\beta}^{ij} = \frac{1}{\Omega} \sum_{\substack{k_{\mu\nu} \\ k_j \neq 0}} \frac{k_\nu k_\mu Z_{j\nu\beta} Z_{i\mu\alpha} e^{-\frac{\eta^2 k^2}{2}}}{\sum_{\alpha\beta} k_\alpha \epsilon_{\alpha\beta} k_\beta} \cos[\mathbf{k}(\mathbf{R}_i - \mathbf{R}_j)] \quad (17)$$

To highlight the long-wavelength limit, we perform the Fourier transform of $\Phi_{\alpha\beta}^{ij}(\mathbf{R}_i, \mathbf{R}_j)$

$$D_{\alpha\beta}^{ij}(\mathbf{q}) = \frac{1}{2\Omega} \sum_{\substack{k_{\mu\nu} \\ \mathbf{k}=\mathbf{q}+\mathbf{G}}} \frac{k_\nu k_\mu Z_{j\nu\beta} Z_{i\mu\alpha} e^{-\frac{\eta^2 k^2}{2}}}{\sum_{\alpha\beta} k_\alpha \epsilon_{\alpha\beta} k_\beta} e^{i\mathbf{k}(\mathbf{R}_i - \mathbf{R}_j)} + \frac{1}{2\Omega} \sum_{\substack{k_{\mu\nu} \\ \mathbf{k}=-\mathbf{q}+\mathbf{G}}} \frac{k_\nu k_\mu Z_{j\nu\beta} Z_{i\mu\alpha} e^{-\frac{\eta^2 k^2}{2}}}{\sum_{\alpha\beta} k_\alpha \epsilon_{\alpha\beta} k_\beta} e^{-i\mathbf{k}(\mathbf{R}_i - \mathbf{R}_j)}. \quad (18)$$

This equation is similar to the *ansatz* employed to perform the Fourier interpolation of phonons in first-principles codes like Quantum ESPRESSO[4, 44, 45] or ABINIT[5, 6, 46] and reproduces the correct $\mathbf{q} \rightarrow 0$ limit when $|\mathbf{G}| \gg \frac{1}{\eta}$:

$$\lim_{\mathbf{q} \rightarrow 0} D_{\alpha\beta}^{ij}(\mathbf{q}) = \frac{1}{\Omega} \frac{\sum_{\mu\nu} Z_{j\nu\beta} q_\nu q_\mu Z_{i\mu\alpha}}{\sum_{\mu\nu} q_\mu \epsilon_{\mu\nu} q_\nu}, \quad (19)$$

which coincides with the standard expression implemented in common electronic-structure packages for the non-analytic part of the force constant matrix (Eq. 18 of Ref. [4]), after the conversion in CGS units where $\epsilon_0 = (4\pi)^{-1}$. Eq. (19) demonstrates that the forces (Eq. 11) and energies (Eq. 9) parametrized by this model correctly reproduce the LO-TO splitting of any materials.

D. Fitting the model

The model can be employed on top of any existing force field. Its application requires the definition of an equilibrium structure where atoms are located in \mathcal{R} , and the dielectric tensor ϵ and the effective charges $Z_{i\alpha\beta}$ computed in this structure. The equilibrium atomic positions \mathcal{R} should ideally correspond to a high symmetry phase, even if it is the saddle point of the energy landscape (with imaginary phonon frequencies). In this way, the energy and its derivatives satisfy all symmetry operations in subgroups of the parent one, thus enabling the potential to respect symmetry constraints of any subgroups. This is relevant in materials where temperature or pressure may change the crystallographic symmetry group by progressively increasing or decreasing the symmetries, like in perovskites, where the cubic $Pm\bar{3}m$ group is a parent of all other symmetry-broken phases. The model's accuracy decreases as the structure deviates from the centroid one, particularly when the effective charges change

significantly. However, in most polar crystals, effective charges are almost independent of the atomic positions as testified by the rarity of multi-phonon scattering modes observed in IR spectra experimentally[47, 48] originated by the dependency of effective charges on the atomic position. This assumption breaks down when simulating liquids, materials where ions diffuse[49], or systems undergoing a significative rearrangement of chemical bonds (strongly first-order phase transitions). In the latter case, separate long-range models for each phase could be employed.

The only free parameter is the cutoff η : the distance below which the long-range interactions are smeared out. The lower η , the smaller the minimum distance between atoms interacting through dipole-dipole electrostatic, thus improving its accuracy. However, the computational cost to evaluate the energy and its derivative increases with low values of η as we need to include more k -points in the summation of Eq. (9). Also, if η is too small, higher orders of the multipole expansion, neglected by the polarization model, become important. Moreover, if the base short-range model has already been fitted, the long-range correction should not affect the training set. This sets a lower bound for η to the maximum distance between any pair of atoms in the training data (accounting for PBC). Thus, the choice of η should be a trade-off between computational cost, required accuracy, and the supercell dimension of the calculations in the training set. If η is smaller than the maximum distance between atoms in the training data, the long-range model energies (Eq. 9), forces (Eq. 11), and stresses alter the training values. In this case, the long-range contribution to the total energy (and derivatives), as evaluated by the model, must be removed from the training data, and the short-range force field must be retrained.

Once \mathcal{R} , $Z_{i\alpha\beta}$, ϵ , and η are established, the final total energy (and its derivatives) of any structure are obtained by adding the ones evaluated by the short-range force field with those of the model.

E. Correcting phonon dispersions in BaTiO₃

Force engines that neglect long-range electrostatic interactions fail to recover the LO-TO splitting near the center of the Brillouin zone, resulting in a crude approximation of phonon dispersions. This is one of the most severe sources of error in short-range force fields when applied to polar materials. We exemplify this issue in the instance of α -BaTiO₃ (cubic perovskite, five atoms in the primitive cell, crystallographic group 221, $Pm\bar{3}m$). Harmonic phonons of this system are characterized by two unstable (imaginary) harmonic phonons across the entire Brillouin zone, as this structure is stabilized by thermal fluctuations at high temperature[50]. In Fig. 1, we report the phonons evaluated within a short-range Gaussian approximation potential (GAP) (Ref. [50]) with and without the addition of the long-range forces (Eq. 11), with

$\eta = 2.5 \text{ \AA}$. As a reference, we plot the first-principles phonon dispersions evaluated within DFPT (with the PBEsol exchange-correlation potential[51], more details on Appendix E), using the same parameters employed to generate the training set of the GAP model. While the GAP already delivers a good agreement with DFPT at the edge of the Brillouin zone, it fails when \mathbf{q} approaches Γ , displaying a significative deviation for some bands already at the halfway point of the Brillouin zone. This is also evident from the zoom-in of the density of states (DOS, right panel of Fig. 1), where a phonon band gap between 500 cm^{-1} and 600 cm^{-1} should separate the highest phonon band from the rest of the phonon dispersions. The short-range GAP does not recover this separation due to merging the LO and TO phonon bands near Γ . On the contrary, the long-range corrected force field qualitatively reproduces the phonon band gap, improving the agreement with DFPT. Another important deviation is observed in the cubic structure's imaginary (unstable) modes. In the short-range model, there is an additional imaginary mode nearby Γ , absent in both the long-range model and the DFPT dispersions.

The chosen value of η (2.5 \AA) slightly modifies the phonon dispersion at the edge of the Brillouin zone, where the \mathbf{q} points are commensurate with the $2 \times 2 \times 2$ supercell employed in the training set of the GAP[50]. If a larger supercell were employed in the training data, the long-range interactions would have significantly altered the phonon dispersion. In the latter case, the energy (and its derivatives) should have been pre-processed by removing the long-range contribution before the training.

III. DISCUSSION

This approach assumes that the dielectric tensor and effective charges are independent of atomic coordinates. This approximation fails when the change in the atomic position breaks covalent bonds or atoms can freely diffuse. Thus, the method is more suited to describe the thermodynamics of structures that keep the same bonding network and topology during the simulation. However, it can still be used to study complex first-order phase transitions when coupled, e.g., with the SSCHA. Within this framework, atoms fluctuate around their centroids, and it is possible to compare the free energies of phases with different bonding networks without breaking any covalent bonds in the simulation, as demonstrated for the study of the γ -Y phase transition in metal-halides perovskites [52] or the hydrogen high-pressure phase-diagram [53].

Overcoming the limitations arising from the model assumptions requires the introduction of the atomic environment dependency on effective charges, dielectric tensors, and centroids. Electric properties like the total polarization, effective charges, and the dielectric tensor are, in fact, routinely parametrized through equivariant machine learning approaches[26, 27], and the centroid pa-

rameter can be rigorously defined through the total polarization and effective charges by inverting Eq. (3). In this way, it is possible to replace in Eq. (9) the explicit dependency of the effective charges, centroids, and dielectric tensor on the atomic positions, similarly as it has been proposed in third and fourth-generation machine learning force fields[17].

We presented a model that can pave the way to a rigorous introduction of long-range electrostatic interaction relying only on physical observables, i.e., without requiring extracting empirical parameters like local atomic charges. This energy-forces-stress model can be combined with existing short-range atomistic potentials, like the GAP shown in Fig. 1[50], to account for long-range electrostatic interactions and further improve their accuracy. The long-range part of energies and forces can be calculated efficiently within Eq. (9) and (11), respectively, and added to the results of short-range models. At the same time, the electrostatic stress tensor is computed by employing the algorithmic differentiation with the procedure explained in Eq. (12,13,14). Only one free parameter needs to be tuned: the smearing η , quantifying the minimum range of the electrostatic interactions. The Born effective charges \mathbf{Z} and the dielectric tensor ϵ are evaluated from first-principles DFPT. The model can correctly account for LO-TO splitting and shines in condensed systems with fixed crystal structures, paving the way to the next-generation machine-learning force fields accounting for long-range electrostatic interactions.

CODE AVAILABILITY

The equations for energy and forces (Eq. 1, Eq. 11) have been implemented in Python and Julia[54] as an open-source package and can be downloaded from <https://github.com/mesonepigreco/electrostatic-calculator>. The stress tensor is evaluated by exploiting the algorithmic differentiation of energy, as implemented in ForwardDiff.jl[42]. The code is distributed under the GPLv3 license. It operates as a force field calculator for the Atomic Simulation Environment[55] (ASE).

DATA AVAILABILITY

All the data reported in this work, such as dynamical matrices, dielectric tensor, and Born effective charges of BaTiO_3 evaluated to produce Fig. 1, are published in the Example folder of the source code GitHub repository.

ACKNOWLEDGMENTS

L. M. acknowledges the H2020 program from the European Union for the MSCA-IF grant 101018714. This work was supported by the Swiss National Supercomputing Centre (CSCS) grant under project ID s1192.

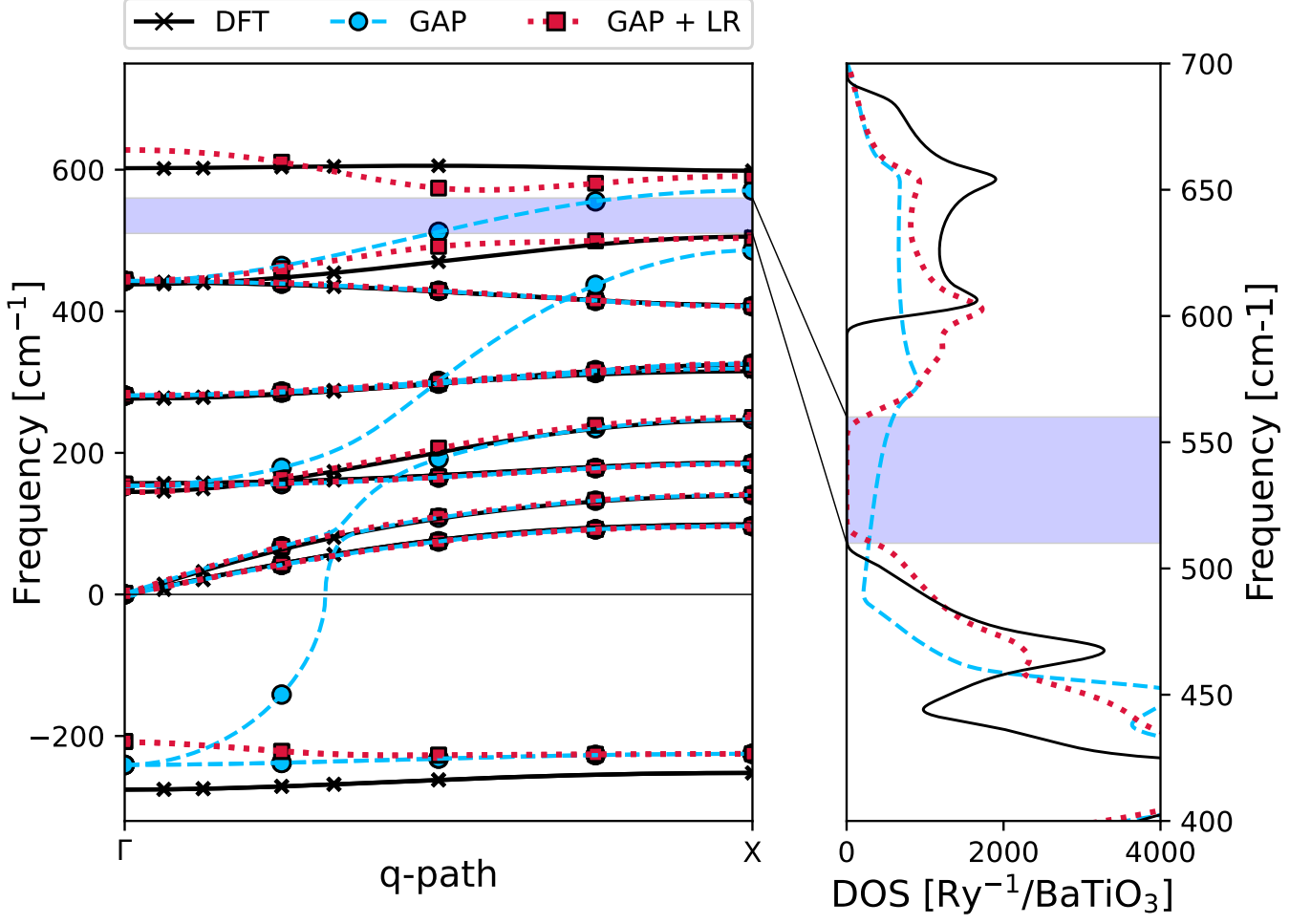


Fig. 1. Phonon band structure of cubic BaTiO₃, comparison between DFT, the GAP without long-range (LR) interaction[50], and the same potential with long-range (LR) interactions adding to the forces Eq. (11). Negative frequencies are imaginary numbers, meaning the structure is on a saddle point of the energy landscape. On the left, we report the dispersion along the $\Gamma - X$ high symmetry line. Scatter points are commensurate with the 8x8x8 supercell employed in the phonon calculation (DFPT calculations are reported with a black cross). The GAP without the long-range interactions fails to describe the phonon bands near Γ . The right panel is a zoom in the high-frequency phonon density of states (DOS), where the two bands above 600 cm⁻¹ and below 500 cm⁻¹ merge in the absence of long-range (LR) interactions. The value of the smearing parameter for the long-range (LR) interactions is $\eta = 2.8 \text{ \AA}$

APPENDICES

Appendix A: Auxiliary system of charges

We need to define a system of charges that satisfy the local dipole moment defined through Eq. (3). For this purpose, for each atom, we generate two charges of opposite sign and modulus q_i , at a distance d so that $\mu_i = q_i d$. The specific choice of q_i and d do not affect the electric field when $r \gg d$, so we have an arbitrary choice for their value. Without loss of generality, we define q_i as the trace of effective charge of the atom i

$$q_i = \frac{1}{3} \sum_{\alpha} Z_{i\alpha\alpha}, \quad (\text{A1})$$

and the position of the positive and negative charges $\tilde{\mathbf{R}}_+$ and $\tilde{\mathbf{R}}_-$ to align the center dipole moment in the middle of the atomic displacement:

$$\tilde{\mathbf{R}}_{i\alpha+} = \mathbf{R}_{i\alpha} + \frac{1}{2q_i} \sum_{\beta} Z_{i\alpha\beta} (\mathbf{R}_{i\beta} - \mathbf{R}_{i\beta}), \quad (\text{A2a})$$

$$\tilde{\mathbf{R}}_{i\alpha-} = \mathbf{R}_{i\alpha} - \frac{1}{2q_i} \sum_{\beta} Z_{i\alpha\beta} (\mathbf{R}_{i\beta} - \mathbf{R}_{i\beta}). \quad (\text{A2b})$$

Appendix B: Electric field

The electric field generated by a charge distribution $\rho(\mathbf{r})$ in a periodic system can be expressed more conveniently in Fourier space transforming the Maxwell relations:

$$\nabla \cdot \mathbf{D} = \rho, \quad (\text{B1})$$

$$\sum_{\alpha\beta} \epsilon_{\alpha\beta} \frac{\partial E_\beta}{\partial r_\alpha} = \frac{\rho}{\epsilon_0}, \quad (\text{B2})$$

$$-\sum_{\alpha\beta} \epsilon_{\alpha\beta} \frac{\partial^2 V}{\partial r_\alpha \partial r_\beta} = \frac{\rho}{\epsilon_0}, \quad (\text{B3})$$

$$-V(\mathbf{k}) \sum_{\alpha\beta} \epsilon_{\alpha\beta} k_\alpha k_\beta = \frac{\rho(\mathbf{k})}{\epsilon_0}, \quad (\text{B4})$$

where $\rho(q)$ is evaluated from the Fourier transform of Eq. (5)

$$\rho(\mathbf{k}) = \frac{1}{\Omega} \int_{\Omega} d\mathbf{r} \sum_i e^{-i\mathbf{k}\cdot\mathbf{r}} \frac{q_i}{\sqrt{8\pi^3\eta^2}} e^{-\frac{(\mathbf{r}-\mathbf{R}_i)^2}{2\eta^2}}. \quad (\text{B5})$$

Here, Ω is the volume of the simulation cell. \mathbf{k} can only assume values so that the integrated function is periodic in \mathbf{r} (reported in Eq. 8). Extending the integral over all the solid volume and dividing by the number of k-points N_k used to sample the Brillouin zone, we can swap the integral and the summation

$$\rho(\mathbf{k}) = \frac{1}{N_k\Omega} \sum_i e^{-i\mathbf{k}\cdot\mathbf{R}_i} \int d\mathbf{r} e^{-i\mathbf{k}\cdot(\mathbf{r}-\mathbf{R}_i)} \frac{q_i}{\sqrt{8\pi^3\eta^2}} e^{-\frac{(\mathbf{r}-\mathbf{R}_i)^2}{2\eta^2}}, \quad (\text{B6})$$

$$\rho(\mathbf{k}) = \frac{1}{N_k\Omega} \sum_i e^{-i\mathbf{k}\cdot\mathbf{R}_i} q_i e^{-\frac{\eta^2 k^2}{2}}. \quad (\text{B7})$$

Exploiting Eq. (B4), one gets the electrostatic potential

$$V(\mathbf{k}) = -\frac{1}{N_k\Omega\epsilon_0} \sum_i \frac{q_i e^{-i\mathbf{k}\cdot\mathbf{R}_i} e^{-\frac{\eta^2 k^2}{2}}}{\sum_{\alpha\beta} k_\alpha \epsilon_{\alpha\beta} k_\beta}, \quad (\text{B8})$$

and the electric field as

$$\mathbf{E}(\mathbf{r}) = -\nabla V(\mathbf{r}), \quad \mathbf{E}(\mathbf{k}) = -i\mathbf{k}V(\mathbf{k}) :$$

$$\mathbf{E}(\mathbf{k}) = \frac{i}{N_k\Omega} \sum_i \frac{q_i \mathbf{k} e^{-i\mathbf{k}\cdot\mathbf{R}_i} e^{-\frac{\eta^2 k^2}{2}}}{\sum_{\alpha\beta} k_\alpha \epsilon_{\alpha\beta} k_\beta}. \quad (\text{B9})$$

To return to real space, we perform the inverse Fourier transform summing over all the k points, excluding the Γ

($\mathbf{k} = 0$), as that term is zero in neutral systems ($\sum_i q_i = 0$):

$$\mathbf{E}(\mathbf{r}) = \frac{i}{N_k\Omega} \sum_{\substack{ij \\ k_j \neq 0}} \frac{q_i \mathbf{k}_j e^{-i\mathbf{k}_j \cdot \mathbf{R}_i} e^{-\frac{\eta^2 k_j^2}{2}}}{\sum_{\alpha\beta} k_{j\alpha} \epsilon_{\alpha\beta} k_{j\beta}} e^{i\mathbf{k}_j \cdot \mathbf{r}}, \quad (\text{B10})$$

$$\mathbf{E}(\mathbf{r}) = \frac{i}{N_k\Omega} \sum_{\substack{ij \\ k_j \neq 0}} \frac{q_i \mathbf{k}_j e^{-\frac{\eta^2 k_j^2}{2}}}{\sum_{\alpha\beta} k_{j\alpha} \epsilon_{\alpha\beta} k_{j\beta}} e^{i\mathbf{k}_j \cdot (\mathbf{r} - \mathbf{R}_i)}. \quad (\text{B11})$$

The sum over i goes on all atoms in all the cells, while j only runs on the cells (the k-points), and the order of the two series can be exchanged thanks to the exclusion of $k_j = 0$. For convenience, we define the charge structure factor as

$$S(\mathbf{k}) = \frac{1}{N_k} \sum_i q_i e^{-i\mathbf{k}\cdot\mathbf{R}_i}. \quad (\text{B12})$$

Since $e^{-i\mathbf{k}\cdot\mathbf{R}_i}$ is invariant if we shift the atomic positions \mathbf{R}_i by a lattice vector, the summation on the atoms i in the supercell is N_k times the one evaluated in the primitive cell only (Eq. (7)). Thus, we get the expression of the electric field

$$\mathbf{E}(\mathbf{r}) = \frac{i}{\Omega} \sum_{\substack{j \\ k_j \neq 0}} \frac{\mathbf{k}_j e^{-\frac{\eta^2 k_j^2}{2}} e^{i\mathbf{k}_j \cdot \mathbf{r}}}{\sum_{\alpha\beta} k_{j\alpha} \epsilon_{\alpha\beta} k_{j\beta}} S(\mathbf{k}_j), \quad (\text{B13})$$

that coincides with the one reported in the main text (Eq. 6).

Appendix C: Expression of the energy

Thanks to Eq. (A1) and (A2), it is possible to build a system of point charges whose positions depend on the atomic coordinates \mathbf{R} and the equilibrium configuration \mathcal{R} .

Substituting the expression of the dipoles (Eq. 3) in the energy Eq. (1), we get:

$$\mathcal{E} = -\frac{1}{2} \sum_{i\alpha\beta} (R_{i\alpha} - \mathcal{R}_{i\alpha}) Z_{i\beta\alpha} E_\beta(\mathbf{R}_i). \quad (\text{C1})$$

where E_β is the β Cartesian component of the electric field on the atom. Substituting the expression of the electric field obtained from the Ewald sum (Eq. 6) into Eq. (C1), we get

$$\begin{aligned} \mathcal{E} = & -\frac{1}{2} \sum_{i\alpha\beta} (R_{i\alpha} - \mathcal{R}_{i\alpha}) \frac{i}{\Omega} \sum_{\substack{k,j \\ k \neq 0}} \frac{Z_{i\beta\alpha} k_\beta e^{-\frac{\eta^2 k^2}{2}}}{\sum_{\mu\nu} k_\mu \epsilon_{\mu\nu} k_\nu} q_j e^{-i\mathbf{k}(\mathbf{R}_j - \mathbf{R}_i)} \\ & \cdot \left[e^{-i \sum_{\mu\nu} \frac{k_\nu Z_{j\nu\mu}}{2q_j} (\mathbf{R}_{j\mu} - \mathcal{R}_{j\mu})} - e^{i \sum_{\mu\nu} \frac{k_\nu Z_{j\nu\mu}}{2q_j} (\mathbf{R}_{j\mu} - \mathcal{R}_{j\mu})} \right]. \end{aligned} \quad (\text{C2})$$

$$\mathcal{E} = \frac{1}{2} \sum_{i\alpha\beta} (R_{i\alpha} - \mathcal{R}_{i\alpha}) \frac{1}{\Omega} \sum_{\substack{k,j \\ k \neq 0}} \frac{Z_{i\beta\alpha} k_\beta e^{-\frac{\eta^2 k^2}{2}}}{\sum_{\mu\nu} k_\mu \epsilon_{\mu\nu} k_\nu} \cdot 2q_j e^{-i\mathbf{k}(\mathbf{R}_j - \mathbf{R}_i)} \sin \left(\sum_{\mu\nu} \frac{k_\nu Z_{j\nu\mu}}{2q_j} (R_{j\mu} - \mathcal{R}_{j\mu}) \right) \quad (\text{C3})$$

Since k is small (constrained by the exponential $e^{-\eta^2 k^2/2}$, where η is large), we expand the sin up to the first order and get Eq. (9):

$$\mathcal{E} = \frac{1}{2} \sum_{ij\alpha\beta\mu\nu} (R_{i\alpha} - \mathcal{R}_{i\alpha})(R_{j\mu} - \mathcal{R}_{j\mu}) \frac{Z_{i\beta\alpha} Z_{j\nu\mu}}{\Omega} \cdot \sum_{\substack{k \\ k \neq 0}} \frac{k_\beta k_\nu e^{-\frac{\eta^2 k^2}{2}}}{\sum_{\mu\nu} k_\mu \epsilon_{\mu\nu} k_\nu} e^{-i\mathbf{k}(\mathbf{R}_j - \mathbf{R}_i)}. \quad (\text{C4})$$

As pointed out in the main text, the dependency from q disappears when expanding the sinus up to the first order, removing any arbitrary choice of the charged system to represent the correct polarization.

Appendix D: Acoustic sum rule

The forces equation (Eq. 11) violates the translational invariance. While the acoustic sum rule in the effective charge prevents a rigid translation of the system from generating a finite dipole moment

$$\sum_i Z_{i\alpha\beta} = 0 \quad \forall \alpha, \beta; \quad (\text{D1})$$

it cannot prevent a global translation from affecting the atomic local dipole $\boldsymbol{\mu}_i$, resulting in a shift of energy and a nonzero net force on the center of mass. To prevent this dependence of the local atomic dipole on global translations, we redefine the centroid position \mathcal{R} to eliminate rigid shifts

$$\mathcal{R}_{i\alpha} = \mathcal{R}_{i\alpha}^{(0)} + \frac{1}{N} \sum_j (R_{j\alpha} - \mathcal{R}_{j\alpha}^{(0)}). \quad (\text{D2})$$

With this redefinition, the overall energy function (Eq. 9) is invariant under global translations. Thus, its derivatives satisfy all the acoustic sum rules. In particular, we show that the actual contribution of this redefinition of the centroid on the forces cancels the force on the center of mass present in Eq. (11):

$$f_{i\alpha}^{\text{ASR}} = - \sum_{j\beta} \frac{\partial \mathcal{E}}{\partial \mathcal{R}_{j\beta}} \frac{\delta_{\beta\alpha}}{N} = \frac{1}{N} \sum_j \frac{\partial \mathcal{E}}{\partial R_{j\alpha}} = - \frac{1}{N} \sum_j f_{j\alpha}. \quad (\text{D3})$$

In the numerical implementation, this expression can be applied *a posteriori* to Eq. (11).

Care must be taken also when computing the stress tensor. In our implementation, since the redefinition of $\mathcal{R}(\mathbf{R})$ (Eq. D2) occurs inside the function that computes the total energy (Eq. 9), the chain rule performed by the algorithmic differentiation automatically includes also the derivatives of the $\mathcal{R}[\mathbf{R}(\boldsymbol{\varepsilon})]$, thus correcting the ASR also for the stress.

Appendix E: Details of the DFT calculation

For the calculation of the DFT phonon spectrum of BaTiO₃ cubic perovskite reported in Fig. 1, as well as for evaluating the effective charges and dielectric tensor, we employed the suite Quantum ESPRESSO[45] version 7.0 within the PBEsol exchange-correlation potential approximation[51]. We used PAW and ultrasoft pseudopotentials from the SSSP library version 1.2.1-efficiency[56], with a cutoff for the wavefunction and density of 60 Ry and 600 Ry, respectively. We sampled the Brillouin zone for the electrons with an 8x8x8 k-mesh without offset. The lattice parameter used for the simulation is 4.035 Å.

-
- [1] L. Binci, P. Barone, and F. Mauri, "First-principles theory of infrared vibrational spectroscopy of metals and semimetals: Application to graphite," *Physical Review B*, vol. 103, no. 13, p. 134304, 2021.
 - [2] G. Marchese, F. Macheda, L. Binci, M. Calandra, P. Barone, and F. Mauri, "Born effective charges and vibrational spectra in superconducting and bad conducting metals," *Nature Physics*, vol. 20, no. 1, pp. 88–94, 2024.
 - [3] W. Cochran and R. A. Cowley, "Dielectric constants and lattice vibrations," *Journal of Physics and Chemistry of Solids*, vol. 23, no. 5, pp. 447–450, 1962.
 - [4] P. Giannozzi, S. de Gironcoli, P. Pavone, and S. Baroni, "Ab initio calculation of phonon dispersions in semiconductors," *Physical Review B*, vol. 43, pp. 7231–7242, Mar. 1991.
 - [5] X. Gonze, J.-C. Charlier, D. Allan, and M. Teter, "Interatomic force constants from first principles: The case of α -quartz," *Physical Review B*, vol. 50, no. 17, pp. 13035–13038, 1994.
 - [6] X. Gonze and C. Lee, "Dynamical matrices, born effective charges, dielectric permittivity tensors, and interatomic force constants from density-functional perturbation theory," *Physical Review B*, vol. 55, no. 16,

- pp. 10355–10368, 1997.
- [7] M. Royo and M. Stengel, “Exact Long-Range Dielectric Screening and Interatomic Force Constants in Quasi-Two-Dimensional Crystals,” *Physical Review X*, vol. 11, p. 041027, Nov. 2021.
 - [8] A. Togo and I. Tanaka, “First principles phonon calculations in materials science,” *Scr. Mater.*, vol. 108, pp. 1–5, Nov 2015.
 - [9] J. Behler, “Perspective: Machine learning potentials for atomistic simulations,” *The Journal of Chemical Physics*, vol. 145, p. 170901, Nov. 2016.
 - [10] K. T. Schütt, P.-J. Kindermans, H. E. Sauceda, S. Chmiela, A. Tkatchenko, and K.-R. Müller, “SchNet: A continuous-filter convolutional neural network for modeling quantum interactions,” 2017.
 - [11] H. Wang, L. Zhang, J. Han, and W. E, “DeePMD-kit: A deep learning package for many-body potential energy representation and molecular dynamics,” *Computer Physics Communications*, vol. 228, pp. 178–184, 2018.
 - [12] V. L. Deringer, A. P. Bartók, N. Bernstein, D. M. Wilkins, M. Ceriotti, and G. Csányi, “Gaussian process regression for materials and molecules,” *Chemical Reviews*, vol. 121, no. 16, pp. 10073–10141, 2021.
 - [13] H. J. Kulik, T. Hammerschmidt, J. Schmidt, S. Botti, M. A. L. Marques, M. Boley, M. Scheffler, M. Todorović, P. Rinke, C. Oses, A. Smolyanyuk, S. Curtarolo, A. Tkatchenko, A. P. Bartók, S. Manzhos, M. Ihara, T. Carrington, J. Behler, O. Isayev, M. Veit, A. Grisafi, J. Nigam, M. Ceriotti, K. T. Schütt, J. Westermayr, M. Gastegger, R. J. Maurer, B. Kalita, K. Burke, R. Nagai, R. Akashi, O. Sugino, J. Hermann, F. Noé, S. Pilati, C. Draxl, M. Kuban, S. Rigamonti, M. Scheidgen, M. Esters, D. Hicks, C. Toher, P. V. Balachandran, I. Tambllyn, S. Whitelam, C. Bellinger, and L. M. Ghiringhelli, “Roadmap on machine learning in electronic structure,” *Electronic Structure*, vol. 4, no. 2, p. 023004, 2022.
 - [14] S. Batzner, A. Musaelian, L. Sun, M. Geiger, J. P. Mailoa, M. Kornbluth, N. Molinari, T. E. Smidt, and B. Kozinsky, “E(3)-equivariant graph neural networks for data-efficient and accurate interatomic potentials,” *Nature Communications*, vol. 13, no. 1, p. 2453, 2022.
 - [15] D. Lu, H. Wang, M. Chen, L. Lin, R. Car, W. E, W. Jia, and L. Zhang, “86 PFLOPS deep potential molecular dynamics simulation of 100 million atoms with ab initio accuracy,” *Computer Physics Communications*, vol. 259, p. 107624, Feb. 2021.
 - [16] A. Musaelian, S. Batzner, A. Johansson, L. Sun, C. J. Owen, M. Kornbluth, and B. Kozinsky, “Learning local equivariant representations for large-scale atomistic dynamics,” *Nature Communications*, vol. 14, Feb. 2023.
 - [17] J. Behler, “Four generations of high-dimensional neural network potentials,” *Chemical Reviews*, vol. 121, p. 10037–10072, Mar. 2021.
 - [18] N. Artrith, T. Morawietz, and J. Behler, “High-dimensional neural-network potentials for multicomponent systems: Applications to zinc oxide,” *Phys. Rev. B*, vol. 83, p. 153101, Apr 2011.
 - [19] A. E. Sifain, N. Lubbers, B. T. Nebgen, J. S. Smith, A. Y. Lohov, O. Isayev, A. E. Roitberg, K. Barros, and S. Tretiak, “Discovering a transferable charge assignment model using machine learning,” *The Journal of Physical Chemistry Letters*, vol. 9, pp. 4495–4501, July 2018.
 - [20] S. A. Ghasemi, A. Hofstetter, S. Saha, and S. Goedecker, “Interatomic potentials for ionic systems with density functional accuracy based on charge densities obtained by a neural network,” *Phys. Rev. B*, vol. 92, p. 045131, Jul 2015.
 - [21] P. Bleiziffer, K. Schaller, and S. Riniker, “Machine learning of partial charges derived from high-quality quantum-mechanical calculations,” *Journal of Chemical Information and Modeling*, vol. 58, pp. 579–590, Feb. 2018.
 - [22] B. Nebgen, N. Lubbers, J. S. Smith, A. E. Sifain, A. Lohov, O. Isayev, A. E. Roitberg, K. Barros, and S. Tretiak, “Transferable dynamic molecular charge assignment using deep neural networks,” *Journal of Chemical Theory and Computation*, vol. 14, pp. 4687–4698, July 2018.
 - [23] K. Yao, J. E. Herr, D. W. Toth, R. Mckintyre, and J. Parkhill, “The TensorMol-0.1 model chemistry: a neural network augmented with long-range physics,” *Chemical Science*, vol. 9, no. 8, pp. 2261–2269, 2018.
 - [24] A. Chandrasekaran, D. Kamal, R. Batra, C. Kim, L. Chen, and R. Ramprasad, “Solving the electronic structure problem with machine learning,” *npj Computational Materials*, vol. 5, Feb. 2019.
 - [25] L. Zhang, H. Wang, M. C. Muniz, A. Z. Panagiotopoulos, R. Car, and W. E, “A deep potential model with long-range electrostatic interactions,” *The Journal of Chemical Physics*, vol. 156, p. 124107, Mar. 2022.
 - [26] M. Gastegger, J. Behler, and P. Marquetand, “Machine learning molecular dynamics for the simulation of infrared spectra,” *Chemical Science*, vol. 8, no. 10, pp. 6924–6935, 2017.
 - [27] A. Grisafi, J. Nigam, and M. Ceriotti, “Multi-scale approach for the prediction of atomic scale properties,” *Chemical Science*, vol. 12, no. 6, p. 2078–2090, 2021.
 - [28] R. D. King-Smith and D. Vanderbilt, “Theory of polarization of crystalline solids,” *Physical Review B*, vol. 47, p. 1651–1654, Jan. 1993.
 - [29] R. Resta, “Macroscopic polarization in crystalline dielectrics: the geometric phase approach,” *Rev. Mod. Phys.*, vol. 66, pp. 899–915, Jul 1994.
 - [30] R. Resta and D. Vanderbilt, *Theory of Polarization: A Modern Approach*, p. 31–68. Springer Berlin Heidelberg.
 - [31] T. W. Ko, J. A. Finkler, S. Goedecker, and J. Behler vol. 12, no. 1, p. 398.
 - [32] Y. Shaidu, F. Pellegrini, E. Küçükbenli, R. Lot, and S. de Gironcoli, “Incorporating long-range electrostatics in neural network potentials via variational charge equilibration from shortsighted ingredients,” vol. 10, no. 1, pp. 1–12.
 - [33] A. Grisafi and M. Ceriotti, “Incorporating long-range physics in atomic-scale machine learning,” *The Journal of Chemical Physics*, vol. 151, p. 204105, Nov. 2019.
 - [34] R. Zubatyuk, J. S. Smith, B. T. Nebgen, S. Tretiak, and O. Isayev, “Teaching a neural network to attach and detach electrons from molecules,” *Nature Communications*, vol. 12, Aug. 2021.
 - [35] T. Sohler, M. Gibertini, M. Calandra, F. Mauri, and N. Marzari, “Breakdown of optical phonons’ splitting in two-dimensional materials,” *Nano Letters*, vol. 17, p. 3758–3763, May 2017.
 - [36] N. Rivano, N. Marzari, and T. Sohler, “Infrared-active phonons in one-dimensional materials and their spectroscopic signatures,” *npj Computational Materials*, vol. 9, Oct. 2023.
 - [37] L. Monacelli, I. Errea, M. Calandra, and F. Mauri, “Pressure and stress tensor of complex anharmonic crystals

- within the stochastic self-consistent harmonic approximation,” *Physical Review B*, vol. 98, p. 024106, July 2018.
- [38] L. Monacelli, R. Bianco, M. Cherubini, M. Calandra, I. Errea, and F. Mauri, “The stochastic self-consistent harmonic approximation: Calculating vibrational properties of materials with full quantum and anharmonic effects,” *Journal of Physics: Condensed Matter*, vol. 33, p. 363001, July 2021.
- [39] L. Monacelli, “Simulating anharmonic crystals: Lights and shadows of first-principles approaches,” vol. 2407.03090.
- [40] A. Siciliano, L. Monacelli, and F. Mauri, “Beyond gaussian fluctuations of quantum anharmonic nuclei,” vol. 110, no. 13, p. 134111.
- [41] M. Miotto and L. Monacelli, “Fast prediction of anharmonic vibrational spectra for complex organic molecules,” vol. 10, no. 1, pp. 1–9.
- [42] J. Revels, M. Lubin, and T. Papamarkou, “Forward-mode automatic differentiation in julia,” 2016.
- [43] T. Sohler, M. Gibertini, M. Calandra, F. Mauri, and N. Marzari, “Breakdown of optical phonons’ splitting in two-dimensional materials,” vol. 17, no. 6, pp. 3758–3763.
- [44] P. Giannozzi, S. Baroni, N. Bonini, M. Calandra, R. Car, C. Cavazzoni, D. Ceresoli, G. L. Chiarotti, M. Cococcioni, I. Dabo, A. D. Corso, S. de Gironcoli, S. Fabris, G. Fratesi, R. Gebauer, U. Gerstmann, C. Gougoussis, A. Kokalj, M. Lazzeri, L. Martin-Samos, N. Marzari, F. Mauri, R. Mazzarello, S. Paolini, A. Pasquarello, L. Paulatto, C. Sbraccia, S. Scandolo, G. Sclauzero, A. P. Seitsonen, A. Smogunov, P. Umari, and R. M. Wentzcovitch, “QUANTUM ESPRESSO: A modular and open-source software project for quantum simulations of materials,” *Journal of Physics: Condensed Matter*, vol. 21, p. 395502, Sept. 2009.
- [45] P. Giannozzi, O. Andreussi, T. Brumme, O. Bunau, M. B. Nardelli, M. Calandra, R. Car, C. Cavazzoni, D. Ceresoli, M. Cococcioni, N. Colonna, I. Carnimeo, A. D. Corso, S. de Gironcoli, P. Delugas, R. A. DiStasio, A. Ferretti, A. Floris, G. Fratesi, G. Fugallo, R. Gebauer, U. Gerstmann, F. Giustino, T. Gorni, J. Jia, M. Kawamura, H.-Y. Ko, A. Kokalj, E. Küçükbenli, M. Lazzeri, M. Marsili, N. Marzari, F. Mauri, N. L. Nguyen, H.-V. Nguyen, A. Otero-de-la-Roza, L. Paulatto, S. Poncé, D. Rocca, R. Sabatini, B. Santra, M. Schlipf, A. P. Seitsonen, A. Smogunov, I. Timrov, T. Thonhauser, P. Umari, N. Vast, X. Wu, and S. Baroni, “Advanced capabilities for materials modelling with Quantum ESPRESSO,” *Journal of Physics: Condensed Matter*, vol. 29, p. 465901, Oct. 2017.
- [46] A. H. Romero, D. C. Allan, B. Amadon, G. Antonius, T. Applencourt, L. Baguet, J. Bieder, F. Bottin, J. Bouchet, E. Bousquet, F. Bruneval, G. Brunin, D. Caliste, M. Côté, J. Denier, C. Dreyer, P. Ghosez, M. Giantomassi, Y. Gillet, O. Gingras, D. R. Hamann, G. Hautier, F. Jollet, G. Jomard, A. Martin, H. P. C. Miranda, F. Naccarato, G. Petretto, N. A. Pike, V. Planes, S. Prokhorenko, T. Rangel, F. Ricci, G.-M. Rignanese, M. Royo, M. Stengel, M. Torrent, M. J. van Setten, B. Van Troeye, M. J. Verstraete, J. Wiktor, J. W. Zwanziger, and X. Gonze, “Abinit: Overview and focus on selected capabilities,” *The Journal of Chemical Physics*, vol. 152, Mar. 2020.
- [47] L. Monacelli and F. Mauri, “Time-dependent self-consistent harmonic approximation: Anharmonic nuclear quantum dynamics and time correlation functions,” *Physical Review B*, vol. 103, p. 104305, Mar. 2021.
- [48] A. Siciliano, L. Monacelli, G. Caldarelli, and F. Mauri, “Wigner gaussian dynamics: Simulating the anharmonic and quantum ionic motion,” *Phys. Rev. B*, vol. 107, p. 174307, May 2023.
- [49] F. Grasselli and S. Baroni, “Topological quantization and gauge invariance of charge transport in liquid insulators,” vol. 15, no. 9, pp. 967–972.
- [50] L. Gigli, M. Veit, M. Kotiuga, G. Pizzi, N. Marzari, and M. Ceriotti, “Thermodynamics and dielectric response of BaTiO₃ by data-driven modeling,” *npj Computational Materials*, vol. 8, pp. 1–17, Sept. 2022.
- [51] J. P. Perdew, A. Ruzsinszky, G. I. Csonka, O. A. Vydrov, G. E. Scuseria, L. A. Constantin, X. Zhou, and K. Burke, “Restoring the density-gradient expansion for exchange in solids and surfaces,” *Physical Review Letters*, vol. 100, p. 136406, Apr. 2008.
- [52] L. Monacelli and N. Marzari, “First-principles thermodynamics of csn₃,” *Chemistry of Materials*, vol. 35, pp. 1702–1709, Feb. 2023.
- [53] L. Monacelli, M. Casula, K. Nakano, S. Sorella, and F. Mauri, “Quantum phase diagram of high-pressure hydrogen,” *Nature Physics*, vol. 19, p. 845–850, Mar. 2023.
- [54] J. Bezanson, A. Edelman, S. Karpinski, and V. B. Shah, “Julia: A fresh approach to numerical computing,” *SIAM review*, vol. 59, no. 1, pp. 65–98, 2017.
- [55] A. H. Larsen, J. J. Mortensen, J. Blomqvist, I. E. Castelli, R. Christensen, M. Dulak, J. Friis, M. N. Groves, B. Hammer, C. Hargus, E. D. Hermes, P. C. Jennings, P. B. Jensen, J. Kermode, J. R. Kitchin, E. L. Kolsbjerg, J. Kubal, K. Kaasbjerg, S. Lysgaard, J. B. Maronsson, T. Maxson, T. Olsen, L. Pastewka, A. Peterson, C. Rostgaard, J. Schiøtz, O. Schütt, M. Strange, K. S. Thygesen, T. Vegge, L. Vilhelmsen, M. Walter, Z. Zeng, and K. W. Jacobsen, “The atomic simulation environment—a python library for working with atoms,” *Journal of Physics: Condensed Matter*, vol. 29, p. 273002, June 2017.
- [56] G. Prandini, A. Marrazzo, I. E. Castelli, N. Mounet, and N. Marzari, “Precision and efficiency in solid-state pseudopotential calculations,” *npj Computational Materials*, vol. 4, Dec. 2018.